Super-resolution Fluorescence Quenching Microscopy of Graphene

Rainer J. Stöhr,[†,*] Roman Kolesov,[†] Kangwei Xia,[†] Rolf Reuter,[†] Jan Meijer,[‡] Gennady Logvenov,[§] and Jörg Wrachtrup[†]

[†]3. Physikalisches Institut, Universität Stuttgart, 70550 Stuttgart, Germany, and Stuttgart Research Center of Photonic Engineering (SCoPE), 70569 Stuttgart, Germany, [‡]RUBION, Ruhr-Universität Bochum, 44780 Bochum, Germany, and [§]Max Planck Institute for Solid State Research, 70569 Stuttgart, Germany

ABSTRACT

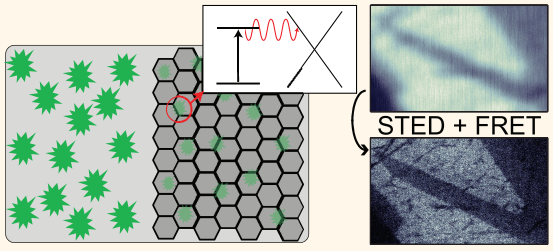

Lately, fluorescence quenching microscopy (FQM) has been introduced as a new tool to visualize graphene-based sheets. Even though quenching of the emission from a dye molecule by fluorescence resonance energy transfer (FRET) to graphene happens on the nanometer scale, the resolution of FQM so far is still limited to several hundreds of nanometers due to the Abbe limit restricting the resolution of conventional light microscopy. In this work, we demonstrate an advancement of FQM by using a super-resolution imaging technique for detecting fluorescence of color centers used in FQM. The technique is similar to stimulated emission depletion microscopy (STED). The combined "FRET+STED" technique introduced here for the first time represents a substantial improvement to FQM since it exhibits in principle unlimited resolution while still using light in the visible spectral range. In the present case we demonstrate all-optical imaging of graphene with resolution below 30 nm. The performance of the technique in terms of imaging resolution and contrast is well described by a theoretical model taking into account the general distance dependence of the FRET process and the distance distribution of donor centers with respect to the flake. In addition, the change in lifetime for partially quenched emitters allows extracting the quenching distance from experimental data for the first time.

KEYWORDS: graphene · fluorescence quenching microscopy · super-resolution imaging · FRET · STED

In recent years, great progress has been made in the field of large-scale production of graphene using either chemical vapor deposition growth on catalytic transition-metal substrates[1−3] or epitaxial growth by high-temperature annealing of SiC.[4−6] At the same time, graphene nanostructures such as graphene nanoribbons or graphene quantum dots are receiving increased attention due to the additional confinement of charge carriers, which results in the appearance of a band gap.[7,8] Such structures are considered as possible candidates for logic device applications in, for example, field effect transistors.[9] The increasing importance of both graphene nanostructures and large-scale graphene raises an inevitable need for microscopy techniques capable of imaging large samples with high spatial resolution. While flakes exfoliated onto Si/SiO_2 substrates can be visualized by means of wide-field optical microscopy, this technique fails on most other substrates as well as for structures smaller than the wavelength of the light used.[10−13] Fluorescence quenching microscopy has therefore been introduced as a techniques capable of imaging graphene and graphene-based sheets such as graphene oxide on a large scale and on arbitrary substrates.[14−16] It relies on the fact that if a fluorescent dipole in an excited state is placed in close proximity to graphene, its fluorescence is quenched due to nonradiative (Förster) resonant energy transfer (FRET).[17] This happens due to the dipole−dipole interaction between the dye molecule and the graphene π-electron system, which returns the donor to its ground state while exciting an electron−hole pair in graphene (see Figure 1B).[18,19] Unlike most other acceptor systems, which permit quenching only in a narrow spectral range, graphene exhibits energy transfer across the entire visible spectrum due to its broadband absorption.[20] Therefore, for super-resolution imaging of graphene, any dye can be used regardless of its emission spectrum. While visualization of graphene based on FQM is known as a high-contrast and high-throughput technique, so far, it does not offer the possibility to resolve features with sizes below the diffraction limit.[16] Here, we demonstrate the combination of FQM with a diffraction-unlimited microscopy technique similar to stimulated emission depletion microscopy

* Address correspondence to r.stoehr@physik.uni-stuttgart.de.

Received for review August 3, 2012 and accepted September 25, 2012.

Published online September 25, 2012
10.1021/nn303510p

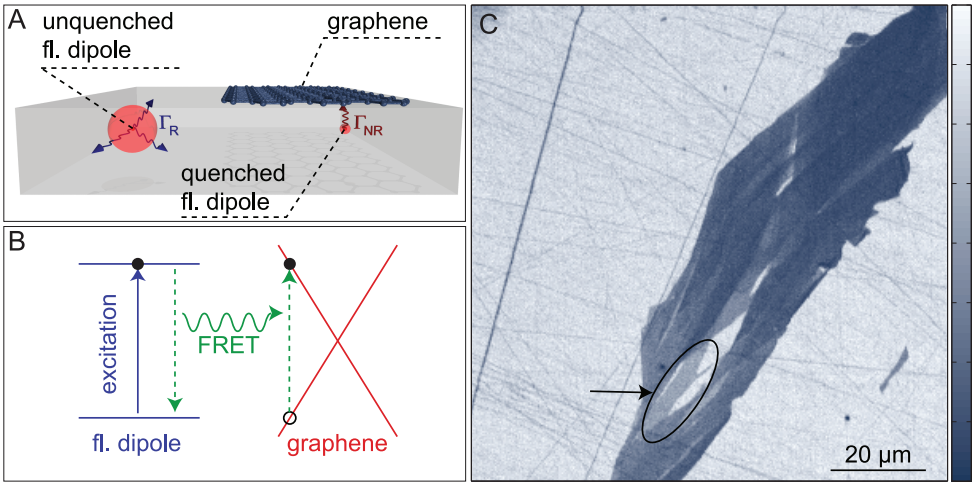

Figure 1. (A) Schematic representation of the sample geometry. Γ_R and Γ_{NR} describes the radiative and nonradiative decay rate, respectively. (B) Simplified Jablonski diagram for the FRET interaction between a fluorescent dipole and graphene. (C) Exfoliated flake on implanted Pr:YAG crystal. The part indicated by the arrow is confirmed to be single-layer graphene using Raman spectroscopy. The image is taken by recording the emission from optically excited Pr^{3+}. The straight lines running across the surface are tiny scratches in the surface of the crystal due to insufficient polishing.

(STED).[21] In principle, STED has no limitation of optical resolution and can be applied to various fluorescent species. The system for which this is demonstrated here is graphene mechanically exfoliated onto praseodymium-implanted yttrium aluminum garnet (Pr:YAG) crystals. The super-resolution microscopy technique relies on two fundamental effects: First is the background-free subdiffraction optical detection of upconverted fluorescence from Pr:YAG, which we have demonstrated in an earlier work.[22] The second is the quenching of Pr:YAG fluorescence by graphene due to fluorescence resonance energy transfer. Here, a resolution below 30 nm is demonstrated. In previous works, we have introduced an imaging technique for multilayer graphene flakes based on the fluorescence of graphene upon pulsed laser excitation.[23] While this technique can be used to visualize graphene with high contrast and unambiguous layer thickness determination, its lateral resolution has a limit on the order of $\lambda/2$ (several hundreds of nanometers in the visible spectral range) due to light diffraction. The same restrictions apply to any other optical imaging techniques such as Raman imaging,[24] FQM,[14] and wide-field light microscopy.[25] Further, we demonstrated subdiffraction all-optical patterning of graphene,[26] although no subdiffraction optical imaging of produced structures was developed. In the following, we show how this deficiency can be resolved by combining STED-like imaging with FQM.

RESULTS AND DISCUSSION

For the proof-of-principles experiment presented here, Pr:YAG is chosen as a donor system for mainly two reasons: First, it is photostable, and, second, its electronic level structure allows for super-resolution microscopy based on a STED-like process.[22] To ensure close spacing between graphene and Pr^{3+} fluorescent ions, praseodymium has been implanted into ultrapure YAG using an energy of 20 keV per positively charged ion followed by annealing at 1200 °C for 24 h. Due to experimental limitations, implantation at lower energies and hence smaller depth was not possible. The resulting implantation depth profile as simulated by SRIM is expected to show a mean implantation depth of around 10.3 nm (see Figure 2A).[27] To further increase FRET efficiency between implanted Pr and graphene, the surface of the YAG crystal was milled down by 6.5 nm using ion milling. The precision of the milling process is limited to roughly ±1 nm.

The measurements presented below rely on the detection of upconverted fluorescence of Pr^{3+} ions, thus allowing for background-free microscopy. Figure 3A shows the electronic structure of Pr^{3+} in YAG. Upconverted UV emission from Pr^{3+} is obtained by a two-step excitation scheme.[28] As a first step, light of 609 nm wavelength excites Pr^{3+} ions from the ground state into the $^1D_2$ state, which has a lifetime of around 200 μs.[29] When adding light of 532 nm wavelength, the system is further excited from the $^1D_2$ state into the 4f5d(1) band, from which strong emission of upconverted UV light occurs.[28] The lifetime of the 4f5d(1) band is roughly 20 ns and therefore significantly shorter than the lifetime of the $^1D_2$ state.[30]

If close to the flake, Pr^{3+} interacts with graphene. The quenching distance (*i.e.*, the Förster radius R_0) is known to be inversely proportional to the fourth power of the transition energy.[31] The transition that is most strongly influenced by FRET is therefore the one between the ground state and the $^1D_2$ state since its energy is much lower compared to the transition from the emitting state. Thus the lifetime of the $^1D_2$ state is expected to shorten significantly, resulting in a lower yield of UV fluorescence. This creates the fluorescence

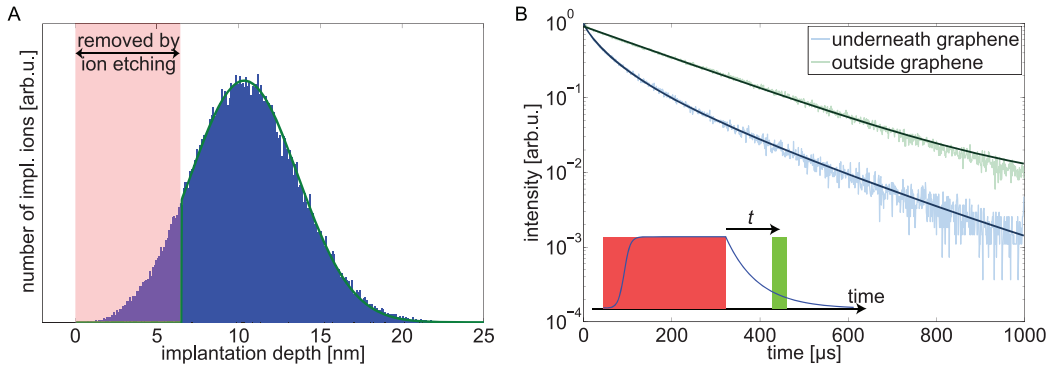

Figure 2. (A) Implantation depth profile of Pr in YAG based on SRIM simulation. After implantation, the YAG surface was etched 6 to 7 nm deep in order to increase FRET efficiency. (B) $^1D_2$-state lifetime with and without fluorescence quenching by graphene. The green line is a fit to the data based on a simple monoexponential decay, resulting in $\Gamma_R = 1/(210\ \mu s)$. The blue line is a fit based on eq 3, from which $R_0 = 11.8$ nm is extracted.

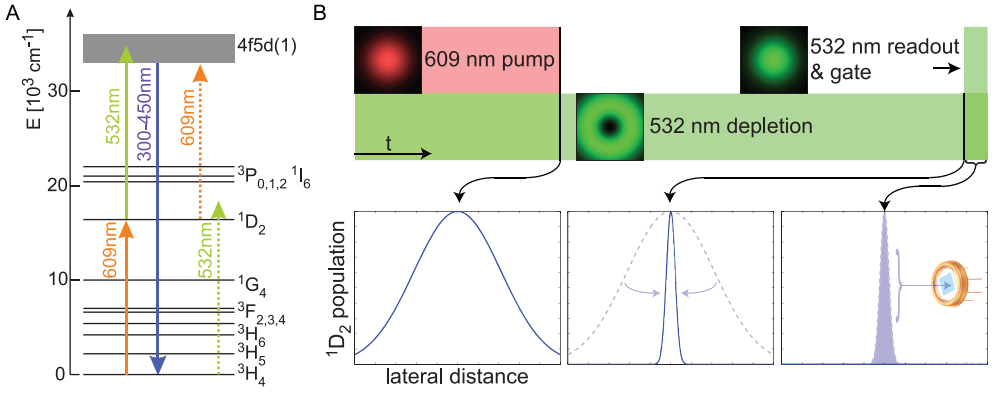

Figure 3. (A) Energy level diagram of Pr^{3+} electronic states in a YAG crystal. The two-step excitation leading to UV fluorescence is indicated by arrows. Note that 532 nm light cannot serve as a first excitation step, and 609 nm cannot serve as a second step. (B) Pulse sequence for super-resolution imaging of graphene. After the first excitation step with 609 nm light, a 532 nm donut beam narrows the spatial distribution of Pr^{3+} centers in the $^1D_2$ state. Finally, a Gaussian 532 nm pulse reads out the remaining $^1D_2$ population. The fluorescence is recorded only during the time of the readout pulse.

contrast between the bare surface and the surface covered with graphene. Figure 1C shows a mechanically exfoliated flake on top of a Pr:YAG crystal imaged by collecting the upconverted UV fluorescence of Pr^{3+} using a home-built confocal microscope. The flake consists of parts of different thicknesses with a single-layer part indicated by the arrow. In the case of a single graphene layer, the Pr^{3+} fluorescence intensity reduces to roughly half compared to the bare surface.

Besides the change in fluorescence intensity as shown in Figure 1C, FRET between Pr^{3+} and graphene can also be witnessed by a change in fluorescence lifetime of the Pr^{3+} emission. The lifetime of the $^1D_2$ state is measured by first applying a 609 nm wavelength pump pulse, exciting the system from the ground state. In order to read out the population in the $^1D_2$ state as a function of time, a 532 nm wavelength readout pulse is applied, with a time variable delay t between the end of the pump pulse and the beginning of the readout pulse. By repeating this sequence for different values of t, the time-dependent population of the $^1D_2$ state and, hence, its lifetime are measured. As shown in Figure 2B, in the unquenched case (measured outside of graphene), the lifetime trace shows a single-exponential decay with a lifetime of roughly 210 μs. This is in good agreement with values reported in the literature to be between 150 and 200 μs.[29] Yet, in the case of fluorescence quenching by graphene, the lifetime is much shorter compared to the unquenched case, and it is strongly multiexponential. The latter is due to the contributions from many Pr^{3+} centers, which are located at different distances to the graphene, as shown by the implantation profile.

The following model is used to describe the dynamics of the $^1D_2$ population in the presence of graphene. The nonradiative decay rate of a single fluorescent center can be calculated by considering the graphene flake as a collection of infinitesimally small "graphene dipoles" covering the entire $x-y$-plane. The general FRET distance dependence predicts that the rate of nonradiative energy transfer from a single fluorescent center to a single "graphene dipole" scales with the sixth power of their mutual distance r.[17] The total nonradiative decay rate Γ_{NR} between the entire graphene flake and a single fluorescent center located at $\vec{r}_c = (x_c, y_c, z_c)$ is obtained by integrating the

contributions from all "graphene dipoles" distributed over the entire surface of the $x-y$-plane located at $z = 0$:

$$\Gamma_{NR} = A\int_{-\infty}^{+\infty} dx \int_{-\infty}^{+\infty} dy \frac{1}{|\vec{r} - \vec{r}_c|^6} = A\int_{-\infty}^{+\infty} dx \int_{-\infty}^{+\infty} dy \frac{1}{\sqrt{(x - x_c)^2 + (y - y_c)^2 + z_c^2}^6} = \Gamma_R \frac{R_0^4}{z_c^4} \quad (1)$$

where A is a proportionality constant and $\Gamma_R = 1/(210\ \mu s)$ is the radiative decay rate of the $^1D_2$ state of Pr^{3+}. The resulting distance dependence of the FRET rate is proportional to the fourth power of the distance between the graphene plane and the emitting dipole. This is in agreement with other theoretical work using a tight-binding model approach.[31] The temporal evolution of the emitted intensity of a single Pr^{3+} center is given by

$$I(t) \propto \frac{\Gamma_R}{\Gamma_R + \Gamma_{NR}} e^{-(\Gamma_R + \Gamma_{NR})t} = \frac{1}{1 + (R_0/z_c)^4} e^{-\Gamma_R(1 + (R_0/z_c)^4)t} \quad (2)$$

To simulate the actual situation, where many centers at different depths are measured simultaneously, eq 2 has to be multiplied by the implantation profile $f(z_c)$ and integrated over z_c:

$$I_{total}(t) \propto \int_0^\infty dz_c \frac{f(z_c)}{1 + (R_0/z_c)^4} e^{-\Gamma_R(1 + (R_0/z_c)^4)t} \quad (3)$$

The implantation profile is taken according to the SRIM simulation shown above by taking into account the milling process and the elevation of the flake above the crystal surface. The latter was obtained in atomic force microscopy (AFM) measurements and appeared to be 1 nm. Although the purity of the crystal is among the highest available for purchase, it still contains traces of residual Pr^{3+}. Its fluorescence is about 60 times lower than that emitted from implanted Pr^{3+}, but for a complete analysis its contribution to the signal is taken into account by adding a z_c-independent offset term to $f(z_c)$. Finally, the only unknown parameter in eq 3 is the Förster radius R_0, which is defined as the distance for which the energy transfer efficiency is 50%. The best fit to the experimental data using eq 3 gives a value of $R_0 \approx 11.8 \pm 1$ nm. The error in R_0 comes primarily from the uncertainty of the milling process. In refs 31 and 18 the quenching factor for single-layer graphene is calculated to be

$$\rho = \frac{\Gamma_R + \Gamma_{NR}}{\Gamma_R} = \frac{\pi\alpha}{16\varepsilon^{5/2}}\left(\frac{c}{v_F}\right)^4 I(z) + 1, \qquad I(z) = \int_0^1 dt\, e^{-2\Delta E z t/\hbar v_F} \frac{t^3}{\sqrt{1 - t^2}} \quad (4)$$

with the fine structure constant α, the Fermi velocity v_F, the vacuum speed of light c, the refractive index $n = \sqrt{\varepsilon}$, the reduced Planck constant $\hbar$, and the energy of the emitted photon ΔE. For a 609 nm transition in YAG ($n = 1.83$), eq 4 leads to a value of $R_0 = 7$ nm, which is slightly lower compared to what is obtained from the experimental data. However, the electronic structure of Pr:YAG is rather complicated since many transitions are involved in the fluorescence process. The Förster radius can therefore not be calculated based on a simple two-level system, although the transition between the ground state and the $^1D_2$ state is expected to be affected most. For a full theoretical treatment, several transitions ($^1D_2 \rightarrow {}^1G_4$, $^3F_{2,3,4}$, $^3H_{4,5,6}$) each experiencing a different degree of quenching would have to be considered. Since the value of $R_0 = 11.8$ nm describes the experimental data very accurately, this value is used for further data analysis.

On the basis of these results, we now turn to super-resolution imaging of graphene. Here, the technique previously used to demonstrate super-resolution upconversion microscopy of praseodymium-doped YAG nanoparticles[22] is adopted for YAG bulk crystals with shallow implanted praseodymium. On the basis of the upconversion excitation scheme mentioned above, super-resolution imaging of Pr:YAG can be arranged in the way schematically indicated in Figure 3B. Three laser beams of different transverse shape (in the sample plane) are used in the timing sequence described below: (1) donut-shaped 532 nm beam shining continuously, (2) Gaussian-shaped chopped 609 nm beam, and (3) Gaussian-shaped chopped 532 nm beam. First, the 609 nm pulse excites the system from the ground state into the $^1D_2$ state. This excitation acts on all Pr^{3+} ions within the entire focal volume. The duration of this pulse needs to be sufficiently long to create a saturated population in the $^1D_2$ state. Here, a value of 5 μs is used at a laser power of 8 mW. After the orange pulse is switched off, two effects influence the population of the $^1D_2$ state: first, a donut-shaped 532 nm depletion beam and, second, FRET with graphene. The donut-shaped 532 nm depletion beam is used to depopulate the $^1D_2$ state by exciting Pr^{3+} from the $^1D_2$ state into the emitting 4f5d(1) band, from where it quickly decays radiatively to the ground state. This depletion beam, however, acts only on the Pr^{3+} ions located around the bright rim of the beam so that the ions close to the center of the beam are not affected. Therefore, during the time this beam acts, the spatial distribution of Pr^{3+} ions, which are still in the $^1D_2$ state, significantly narrows around the center of the beam. The last part of the pulse sequence is a short Gaussian-shaped 532 nm readout pulse. This pulse transfers all the population remaining in the $^1D_2$ state into the emitting 4f5d(1) band. To obtain super-resolution, only the Pr^{3+} UV fluorescence emitted during the duration of the readout pulse is recorded, while all other emission is discarded. In that way, the recorded fluorescence originates from a spot much smaller than the diffraction-limited excitation. The time

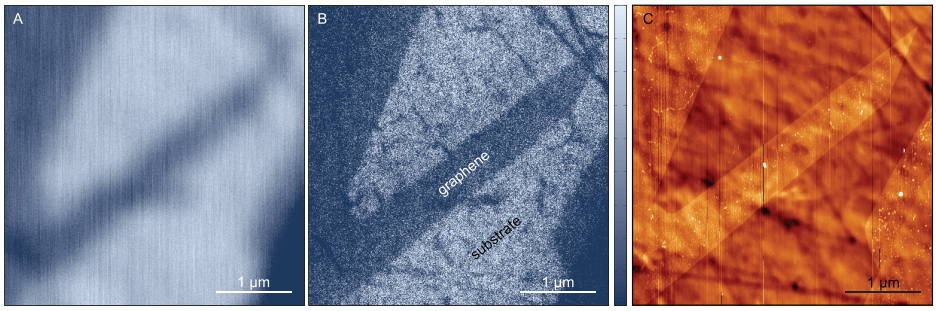

Figure 4. Super-resolution imaging of graphene by "FRET+STED". (A) By using only 609 nm pump and 532 nm readout pulses, the resolution is given essentially by the Abbe limit. (B) Adding an additional 532 nm donut-shaped depletion beam, super-resolution imaging of graphene is obtained. (C) AFM image of the same region.

between the end of the orange pump pulse and the beginning of the green readout pulse has to be chosen according to the following considerations. First, the donut-shaped depletion beam needs to act long enough to efficiently narrow the spatial distribution of Pr^{3+} ions in the $^1D_2$ state. This time can in principle be decreased by increasing the power of the beam. While longer time as well as higher power immediately improves the resolution, it also decreases the signal strength since fewer Pr^{3+} ions are left in the $^1D_2$ state and read out by the readout pulse. At the same time, the duration needs to be long enough to allow graphene to efficiently quench the $^1D_2$ state of Pr^{3+}, while the unquenched ions outside graphene should not have decayed too much. Experimentally, the best compromise among good resolution, good signal strength, and high FRET contrast is found for a time of $\tau = 33\ \mu s$ between the pump and readout pulse at a laser power of 55 mW (see Supporting Information). A duration of 1 μs for the readout pulse is sufficient to read out all the population left in the $^1D_2$ state using 6 mW of green readout power.

Figure 4 shows a closeup of the single-layer flake. In Figure 4A, no depleting 532 nm donut beam is used so that the resolution is essentially given by the general Abbe limit of optical microscopy. Yet, when adding the depletion beam, super-resolution imaging is achieved (Figure 4B). The resolution of the image can be obtained by measuring the fluorescence intensity across a step between graphene and the bare substrate. For this case, the nonradiative decay rate Γ_{NR} between graphene and Pr^{3+} is calculated analogously to eq 1 by assuming that graphene covers only half the surface so that the step is along the $x = 0$ line:

$$\begin{aligned}\Gamma_{NR} &= A\int_{-\infty}^{0} dx \int_{-\infty}^{+\infty} dy \frac{1}{|\vec{r} - \vec{r}_c|^6} \\ &= A\int_{-\infty}^{0} dx \int_{-\infty}^{+\infty} dy \frac{1}{\sqrt{(x - x_c)^2 + (y - y_c)^2 + z_c^2}^6} \\ &= \Gamma_R \frac{\pi R_0^4 (2x_c^3 + 3x_c z_c^2 + 2x_c^2\sqrt{x_c^2 + z_c^2} + 2z_c^2\sqrt{x_c^2 + z_c^2})}{8z_c^4 (x_c^2 + z_c^2)^{3/2}}\end{aligned} \quad (5)$$

Analogously to eq 3, the implantation profile is taken into account by multiplying with the Pr^{3+} distribution function $f(z_c)$ and integrating over z_c. Further, due to the finite size of the laser spot, contributions from many centers located around the focus point have to be included when calculating the fluorescence intensity across the step. For that, a Gaussian point-spread function with a width of R_{Laser} is assumed:

$$g(x_c, y_c) = e^{-((x - x_c)^2 + (y - y_c)^2)/R_{Laser}^2} \quad (6)$$

This describes also the case of super-resolution imaging where the resolution can be expressed by an effective laser spot size given by the depletion process. Overall, the emission intensity is calculated by integrating over the contributions from the ion distribution profile $f(z_c)$ and the lateral point-spread function $g(x_c,y_c)$:

$$I_{total}(x, y) \propto \int_{-\infty}^{+\infty} dx_c \int_{-\infty}^{+\infty} dy_c \int_{-\infty}^{0} dz_c \frac{e^{-(\Gamma_R + \Gamma_{NR})\tau}}{1 + (R_0/z_c)^4} f(z_c)\, g(x_c, y_c) \quad (7)$$

where $\tau = 33\ \mu s$ is the waiting time between the end of the orange pump pulse and the beginning of the green readout pulse. For the case where $R_{Laser} \gg R_0$, FRET effects play a subordinate role in the width of the step. In this case, the resolution is determined solely by the effective laser spot size given by the STED-like technique. Only once R_{Laser} becomes comparable to R_0 does the Förster radius limit the sharpness of the step. Figure 5A shows the experimentally obtained intensity trace across the graphene-substrate step together with three traces calculated according to eq 7 using different values for the laser spot size. The experimental curve is obtained by averaging several lines across the step. All curves are normalized from 0 to 1. A value of R_{Laser} = 30 nm gives roughly the best agreement between the model and the experimental data. The difference between the experimental values and the model based on these parameters is shown in the residual plot at the bottom of Figure 5A. The fact that the residuals behave randomly and do not show any distinct features confirms the validity of the model. The performance of this combined FRET+STED technique

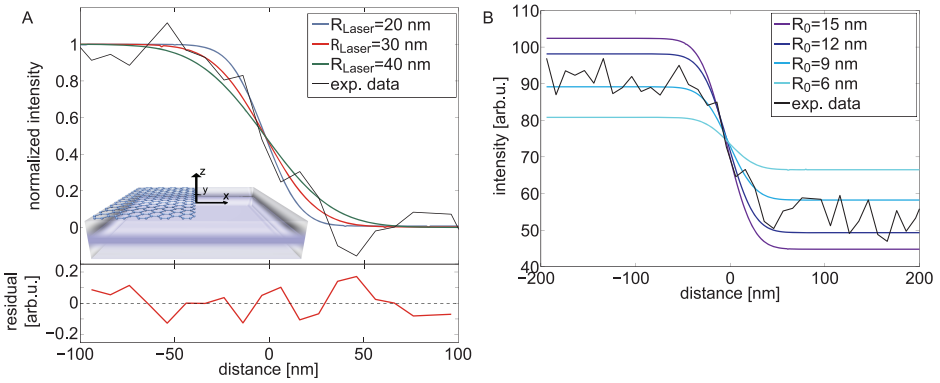

Figure 5. (A) Normalized step width for different values of R_{Laser}. The best agreement with the data is obtained for $R_{Laser} \approx$ 30 nm. While for R_{Laser} = 20 nm and R_{Laser} = 40 nm the sum of the squared errors is 0.21 and 0.2 nm^2, respectively, it is 0.15 nm^2 for R_{Laser} = 30 nm. The quenching radius is set at 11.8 nm in all cases. The inset shows the sample geometry as used throughout eqs 5−7. The residual plot at the bottom confirms the overall validity of the model. (B) Several traces for different values of R_0 resulting in different contrast. The best agreement with the experimental data is for $R_0 \approx$ 10 nm. The laser spot size is set to be 30 nm in all cases.

can therefore be considered to be equivalent with that of an imaginary optical microscope where the excitation light is focused into a 30 nm spot (Gaussian half-width). This is in good agreement with measurements on structured implantation where the transition between implanted and nonimplanted regions is resolved with 35 nm precision (see Supporting Information). Finally, Figure 5B shows the imaging contrast for single-layer graphene for different values of the Förster radius together with the experimental data. The Förster radius has a direct influence on the contrast of the step since, for larger R_0, quenching becomes more efficient, resulting in a larger intensity difference between quenched and unquenched regions. For R_0 = 11.8 nm as obtained from the lifetime fit above, the contrast is expected to be slightly better compared to what is obtained experimentally. Yet, in the experimental situation, the contrast can be spoiled by, for example, background contributions due to impurities, incomplete rejection of laser light by the optical filters, or dark counts from the detectors. Considering this, the model still reproduces the experimental data quite well.

CONCLUSIONS

In summary, we demonstrate here for the first time an optical technique combining super-resolution imaging with fluorescence quenching microscopy. This technique was applied to imaging graphene on top of a YAG crystal shallow implanted with Pr^{3+}, resulting in lateral resolution below 30 nm. Furthermore, a Förster radius of 11.8 ± 1 nm is extracted from the lifetime of partially quenched emitters. While here, graphene was imaged on top of an implanted crystal; the same technique can be applied to graphene covered by a thin film of a fluorescent dye such as rhodamine. In addition, instead of using a STED-like technique for super-resolution imaging, other methods such as photoactivated localization microscopy (PALM) or stochastic optical reconstruction microscopy (STORM) can be used, which would allow for wide-field imaging rather than point-by-point raster scanning. This would increase the imaging throughput dramatically. Furthermore, increasing the resolution further to below 10 nm might allow directly measuring the quenching radius from the width of the step between the graphene and the bare substrate. Finally, by functionalizing an AFM tip with a fluorescent dye, FQM can be incorporated into a scanning-probe technique. This would offer a variety of metrological applications such as probing local density of states.

EXPERIMENTAL SECTION

Measurements were performed in a home-built confocal microscope (see Supporting Information). A rhodamine 6G dye laser was used as an orange excitation source, while a diode-pumped solid-state laser was used for 532 nm excitation. The orange and green readout laser beams were passed through a single-mode optical fiber to ensure their Gaussian beam profile. The donut-shaped depleting beam was obtained by passing the Gaussian beam through a vortex phase shifting plate. All beams were spatially overlapped and sent onto the sample through a 1.3 NA oil immersion objective mounted on a three-dimensional nanopositioning piezo stage. The same objective was used to collect the emitted UV light, which afterward was filtered spectrally with a 450 nm short-pass filter and sent onto a UV-sensitive single-photon-counting photomultiplier tube.

Conflict of Interest: The authors declare no competing financial interest.

Acknowledgment. The authors thank Benjamin Stuhlhofer for technical support. Financial support by MPG Fellowship and EU SQUTEC is also acknowledged.

Supporting Information Available: Detailed description of the experimental setup. Resolution determination on patterned implantation. Determination of the pulse sequence timing. This material is available free of charge *via* the Internet at http://pubs.acs.org.

REFERENCES AND NOTES

1. Kim, K. S.; Zhao, Y.; Jang, H.; Lee, S. Y.; Kim, J. M.; Kim, K. S.; Ahn, J.-H.; Kim, P.; Choi, J.-Y.; Hong, B. H. Large-Scale Pattern Growth of Graphene Films for Stretchable Transparent Electrodes. *Nature* **2009**, *457*, 706–710.
2. Li, X.; Cai, W.; An, J.; Kim, S.; Nah, J.; Yang, D.; Piner, R.; Velamakanni, A.; Jung, I.; Tutuc, E.; *et al*. Large-Area Synthesis of High-Quality and Uniform Graphene Films on Copper Foils. *Science* **2009**, *324*, 1312–1314.
3. Reina, A.; Jia, X.; Ho, J.; Nezich, D.; Son, H.; Bulovic, V.; Dresselhaus, M. S.; Kong, J. Large Area, Few-Layer Graphene Films on Arbitrary Substrates by Chemical Vapor Deposition. *Nano Lett.* **2009**, *9*, 30–35.
4. Emtsev, K. V.; Bostwick, A.; Horn, K.; Jobst, J.; Kellogg, G. L.; Ley, L.; McChesney, J. L.; Ohta, T.; Reshanov, S. A.; Rohrl, J.; *et al*. Towards Wafer-Size Graphene Layers by Atmospheric Pressure Graphitization of Silicon Carbide. *Nat. Mater.* **2009**, *8*, 203–207.
5. Berger, C.; Song, Z.; Li, X.; Wu, X.; Brown, N.; Naud, C.; Mayou, D.; Li, T.; Hass, J.; Marchenkov, A. N.; *et al*. Electronic Confinement and Coherence in Patterned Epitaxial Graphene. *Science* **2006**, *312*, 1191–1196.
6. Ohta, T.; Bostwick, A.; Seyller, T.; Horn, K.; Rotenberg, E. Controlling the Electronic Structure of Bilayer Graphene. *Science* **2006**, *313*, 951–954.
7. Han, M. Y.; Özyilmaz, B.; Zhang, Y.; Kim, P. Energy Band-Gap Engineering of Graphene Nanoribbons. *Phys. Rev. Lett.* **2007**, *98*, 206805.
8. Son, Y.-W.; Cohen, M. L.; Louie, S. G. Energy Gaps in Graphene Nanoribbons. *Phys. Rev. Lett.* **2006**, *97*, 216803.
9. Wang, X.; Ouyang, Y.; Li, X.; Wang, H.; Guo, J.; Dai, H. Room-Temperature All-Semiconducting Sub-10-nm Graphene Nanoribbon Field-Effect Transistors. *Phys. Rev. Lett.* **2008**, *100*, 206803.
10. Ni, Z. H.; Wang, H. M.; Kasim, J.; Fan, H. M.; Yu, T.; Wu, Y. H.; Feng, Y. P.; Shen, Z. X. Graphene Thickness Determination Using Reflection and Contrast Spectroscopy. *Nano Lett.* **2007**, *7*, 2758–2763.
11. Blake, P.; Hill, E. W.; Neto, A. H. C.; Novoselov, K. S.; Jiang, D.; Yang, R.; Booth, T. J.; Geim, A. K. Making Graphene Visible. *Appl. Phys. Lett.* **2007**, *91*, 063124.
12. Abergel, D. S. L.; Russell, A.; Fal'ko, V. I. Visibility of Graphene Flakes on a Dielectric Substrate. *Appl. Phys. Lett.* **2007**, *91*, 063125.
13. Jung, I.; Pelton, M.; Piner, R.; Dikin, D. A.; Stankovich, S.; Watcharotone, S.; Hausner, M.; Ruoff, R. S. Simple Approach for High-Contrast Optical Imaging and Characterization of Graphene-Based Sheets. *Nano Lett.* **2007**, *7*, 3569–3575.
14. Treossi, E.; Melucci, M.; Liscio, A.; Gazzano, M.; Samori, P.; Palermo, V. High-Contrast Visualization of Graphene Oxide on Dye-Sensitized Glass, Quartz, and Silicon by Fluorescence Quenching. *J. Am. Chem. Soc.* **2009**, *131*, 15576–15577.
15. Kim, J.; Cote, L. J.; Kim, F.; Huang, J. Visualizing Graphene Based Sheets by Fluorescence Quenching Microscopy. *J. Am. Chem. Soc.* **2010**, *132*, 260–267.
16. Kyle, J. R.; Guvenc, A.; Wang, W.; Ghazinejad, M.; Lin, J.; Guo, S.; Ozkan, C. S.; Ozkan, M. Centimeter-Scale High-Resolution Metrology of Entire CVD-Grown Graphene Sheets. *Small* **2011**, *7*, 2599–2606.
17. Forster, T. Zwischenmolekulare Energiewanderung und Fluoreszenz. *Ann. Phys.* **1948**, *2*, 55–75.
18. Chen, Z.; Berciaud, S.; Nuckolls, C.; Heinz, T. F.; Brus, L. E. Energy Transfer from Individual Semiconductor Nanocrystals to Graphene. *ACS Nano* **2010**, *4*, 2964–2968.
19. Gómez-Santos, G.; Stauber, T. Fluorescence Quenching in Graphene: A Fundamental Ruler and Evidence for Transverse Plasmons. *Phys. Rev. B* **2011**, *84*, 165438.
20. Mak, K. F.; Sfeir, M. Y.; Wu, Y.; Lui, C. H.; Misewich, J. A.; Heinz, T. F. Measurement of the Optical Conductivity of Graphene. *Phys. Rev. Lett.* **2008**, *101*, 196405.
21. Hell, S. W.; Wichmann, J. Breaking the Diffraction Resolution Limit by Stimulated Emission: Stimulated-Emission-Depletion Fluorescence Microscopy. *Opt. Lett.* **1994**, *19*, 780–782.
22. Kolesov, R.; Reuter, R.; Xia, K.; Stöhr, R.; Zappe, A.; Wrachtrup, J. Super-Resolution Upconversion Microscopy of Praseodymium-Doped Yttrium Aluminum Garnet Nanoparticles. *Phys. Rev. B* **2011**, *84*, 153413.
23. Stöhr, R. J.; Kolesov, R.; Pflaum, J.; Wrachtrup, J. Fluorescence of Laser-Created Electron-Hole Plasma in Graphene. *Phys. Rev. B* **2010**, *82*, 121408.
24. Graf, D.; Molitor, F.; Ensslin, K.; Stampfer, C.; Jungen, A.; Hierold, C.; Wirtz, L. Spatially Resolved Raman Spectroscopy of Single- and Few-Layer Graphene. *Nano Lett.* **2007**, *7*, 238–242.
25. Novoselov, K. S.; Jiang, D.; Schedin, F.; Booth, T. J.; Khotkevich, V. V.; Morozov, S. V.; Geim, A. K. Two-Dimensional Atomic Crystals. *Proc. Natl. Acad. Sci. U. S. A.* **2005**, *102*, 10451–10453.
26. Stöhr, R. J.; Kolesov, R.; Xia, K.; Wrachtrup, J. All-Optical High-Resolution Nanopatterning and 3D Suspending of Graphene. *ACS Nano* **2011**, *5*, 5141–5150.
27. Ziegler, J. F.; Ziegler, M.; Biersack, J. SRIM - The Stopping and Range of Ions in Matter. *Nucl. Instrum. Methods Phys. Res., Sect. B* **2010**, *268*, 1818–1823.
28. Gayen, S. K.; Xie, B. Q.; Cheung, Y. M. Two-Photon Excitation of the Lowest $4f^2 \rightarrow 4f5d$ Near-Ultraviolet Transitions in $Pr^{3+}:Y_3Al_5O_{12}$. *Phys. Rev. B* **1992**, *45*, 20–28.
29. Özen, G.; Forte, O.; Bartolo, B. D. Upconversion Dynamics in Pr-Doped $YAlO_3$ and $Y_3Al_5O_{12}$ Laser Crystals. *Opt. Mater. (Amsterdam, Neth.)* **2005**, *27*, 1664–1671.
30. Weber, M. Nonradiative Decay from 5d States of Rare Earths in Crystals. *Solid State Commun.* **1973**, *12*, 741–744.
31. Swathi, R. S.; Sebastian, K. L. Long Range Resonance Energy Transfer from a Dye Molecule to Graphene Has (Distance)$^{-4}$ Dependence. *J. Chem. Phys.* **2009**, *130*, 086101.